PREPRINT UCRL- 77357

CONF-751026--20

Lawrence Livermore Laboratory

DT FUSION NEUTRON RADIATION STRENGTHENING OF COPPER AND NIOBIUM

J. B. Mitchell, R. A. Van Konynenburg, C. J. Echer - LLL

D. M. Parkin - LASL

September 29, 1975

Int'l Conf on Radiation Effects and Tritium Technology for Fusion Reactors
October 1-3, 1975 Gatlinburg, TN

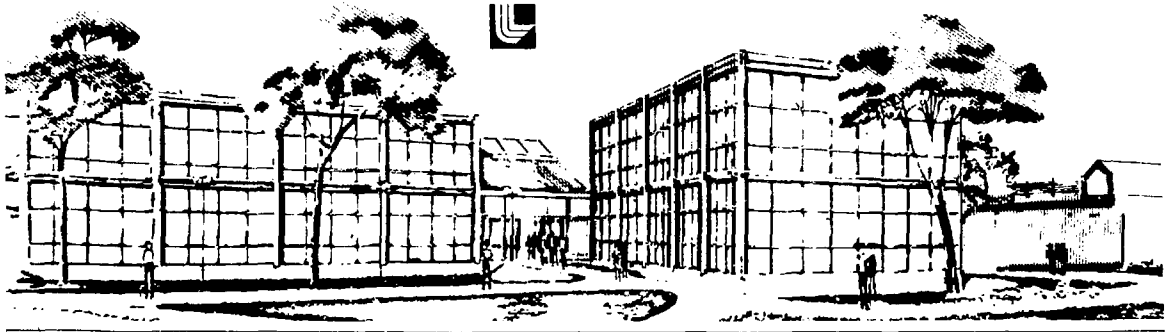

DT FUSION NEUTRON RADIATION STRENGTHENING OF COPPER AND NIOBIUM

J. B. Mitchell
D. M. Parkin*
R. A. Van Konynenburg
C. J. Echer

MEETING:

International Conference on Radiation Effects and Tritium Technology for Fusion Reactors

October 1-3, 1975

Riverside Motor Lodge
Gatlinburg, Tennessee

*Los Alamos Scientific Laboratory, Los Al[illegible] .M

DT FUSION NEUTRON RADIATION STRENGTHENING OF COPPER AND NIOBIUM

J. B. Mitchell* D. H. Parkin+
R. A. Van Konynenburg* C. J. Echer*

*Lawrence Livermore Laboratory, Livermore, CA
+Los Alamos Scientific Laboratory, Los Alamos, NM

ABSTRACT

The initial results of a comparative study of the radiation strengthening and damage structures produced in Cu and Nb by D-T fusion and fission reactor neutrons are described. The radiation strengthening produced by a given fluence of fusion neutrons above about 10^{17}n/cm^2 is equal to that produced by a fluence of fission reactor neutrons (E >0.1 MeV) ten times as great. This difference is about twice as large as would be expected if the strengthening scaled with damage energy or dpa. Initial transmission electron microscopy observations of the damage structures in fusion and fission reactor neutron irradiated copper indicate that the same type of primary structural defects, vacancy and interstitial point defect clusters and small dislocation loops with a/3 ⟨111⟩ and a/2 ⟨110⟩ Burgers vectors, are produced in both cases. The difference in the radiation strengthening produced by fusion and fission reactor neutrons in Cu appears to result from a substantially greater rate of accumulation of damage, in the form of point defect clusters, during irradiation with fusion neutrons than during irradiation with fission reactor neutrons plus a significant difference in the size and spatial distributions of the damage clusters.

INTRODUCTION

The recent growth of interest in controlled thermonuclear reactor (CTR) technology has generated considerable discussion of the effects of 14 MeV D-T fusion neutron radiation damage on candidate structural materials for fusion reactors.

Because experimental facilities that [illegible] 14 MeV neutron fluxes and fluences comparable to those expected in a fusion reactor do not exist and appear unlikely to be developed in the near future, much of the current effort is being directed toward theoretical predictions and experimental simulations of D-T fusion neutron damage effects.

Theoretical studies have shown that the displacement damage resulting from Frenkel pair generation produced by 14 MeV fusion neutrons in metals such as Cu and Nb should be about 4 to 6 times as great as that produced by the same fluence of fission reactor neutrons. Inspection of (n,α) cross sections for different neutron energies indicates that the rate of internal helium generation could be a hundred to a thousand times as great during fusion neutron irradiation as during irradiation with the same flux of fission neutrons

Simulation experiments are directed toward producing the same quantities of displacement damage, in terms of damage energy or displacements per atom (dpa), expected from a given fluence of fusion neutrons by irradiation with high-energy ions or fission reactor neutrons. Internal helium quantities comparable to those expected from fusion neutron (n,α) reactions are produced by alpha particle injection, (n,α) reactions in certain materials using high thermal neutron fluxes or by the radioactive decay of dissolved tritium. In most simulations the effects of damage generation rates and possible synergistic effects of damage components are ignored or estimated using classical kinetic and thermodynamic models of damage structure development.

Implicit in these simulation efforts is the assumption that the same processes that determine the nature and distribution of the resultant damage structure and associated physical and mechanical properties under the simulation conditions are also dominant during radiation with fusion neutrons, and that at elevated temperatures and higher damage states they will produce the same effects.

Clearly, one would like to establish confidence in the validity of these simulations by [illegible] effects with the effects produced under equivalent conditions by high fluences ($\sim 10^{23}$ n/cm^2) of fusion

neutrons. However, because of the earlier mentioned limitations on fusion neutron flux and fluence this does not appear to be possible in the foreseeable future.

Some insight into the credibility of some of the aspects of fission reactor neutron simulations of fusion neutron radiation effects can be gained by comparision of the structure and properties produced in a material during irradiation over the fluences within the practical limitation of the Rotating Target Neutron Source (RTNS) at the Lawrence Livermore Laboratory.

Radiation damage experiments on the RTNS can be conducted on small specimens over a wide range of temperatures and environmental conditions in a D-T fusion neutron flux up to approximately 10^{12} n/cm^2-sec and at practical fluence levels up to 10^{18} n/cm^2. These experiments, although not generally useful for yielding engineering design data, can provide a basic understanding of the nature and effects of fusion neutron damage and increased confidence in the predictions and simulations by other sources of radiation damage.

In addition to providing specimens for direct vacuum fusion mass spectroscopy measurements of rates of helium generation in metals and alloys during fusion neutron irradiation, one can also conduct studies to verify the theoretically predicted ratios of displacement damage rates produced by fusion and fission reactor neutrons. Direct comparisons of the resultant physical and mechanical property changes produced by fusion and fission reactor neutron irradiation can be made to determine the validity of the damage energy or dpa criterion for property change simulation.

Finally, an evaluation of the resultant damage structures can be made to assess any differences in the nature, quantities, and distribution of the damage in fusion and fission reactor neutron irradiated materials and to determine if the same or different processes are dominant in determining the resultant structures.

The work described in this paper examines and compares the effect of fusion and fission reactor neutron irradiations on the tensile yield strength and resultant displacement damage structures in copper and niobium.

EXPERIMENTAL PROCEDURE

Sample Preparation

Small tensile samples of Cu and Nb of dimensions shown in Figure 1 were machined from 0.5 mm (0.020-inch) thick cold-rolled sheet stock from LLL stores and from higher purity material purchased from MRC and Cominco[†]. The chemical analyses of these materials are shown in Table 1.

The Nb tensile samples were annealed for 1 hour at 1200°C in 0.13 mPa ($\approx 10^{-9}$ torr) vacuum and the Cu samples for 1 hour at 600°C in ≈1.3 mPa (10^{-5} torr) vacuum. These times and temperatures were used to obtain grain sizes that would give at least 10 grains over the 0.5 mm (0.020-inch) thickness to insure reproducible polycrystalline tensile behavior. Representative photos of the annealed grain structures are shown in Figures 2 and 3 for Nb and Cu, respectively.

The tensile samples were then encapsulated for irradiation in the Rotating Target Neutron Source (RTNS) and the Livermore Pool Type Reactor (LPTR) as described in the next section.

Irradiation Facilities, Neutron Spectra, Dosimetry, Encapsulation, and Temperature Control

A. Rotating Target Neutron Source (RTNS)

The RTNS has been described in detail elsewhere[1-5]. Essentially, it consists of an accelerator which produces a beam of 400 keV deuterons and a tritium-loaded titanium target in which fusion reactions take place and from which neutrons are emitted. The actual neutron-emitting region of the target can be approximated as a disc with a diameter of about one centimeter and negligible thickness. The small size of the tensile samples was dictated in part by the size of this target disc and the fact that the neutrons are emitted nearly isotropically in the

laboratory coordinate system, which leads to a rapid decrease of the flux with distance away from the source.

The energy of a neutron emitted by a DT fusion accelerator source depends on the energy of the deuteron at the time it enters into the reaction and the angle between the path of the incoming deuteron and the path of the emitted neutron. In the RTNS, the target is thicker than the deuteron range, so that the deuteron energy at the time of reaction can lie between 400 keV and 15 keV or less. Because of this spread in deuteron energies, the neutrons emitted in the forward direction can have energies between 13.0 and 13.6 MeV, according to calculations involving

Table 1. Chemical Analyses of Impurity Elements in Copper and Interstitial Impurities in Niobium

	LLL Stores Grade	Comineo
COPPER		
Element:		
Fe	300 ppm	400 ppm
Si	100 ppm	150 ppm
Mg	4 ppm	10 ppm
Ag	50 ppm	2 ppm
Ca	25 ppm	2 ppm
Co	<10 ppm	<10 ppm
Ni	5 ppm	<3 ppm
Al	<3 ppm	<3 ppm
Be	30 ppm	<1 ppm
NIOBIUM		
LLL Stores Grade		Comineo
C	15	15 ppm
O	30S	40 ppm
N	70	5 ppm

conservation of energy and momentum[6]. There is also a range in the angle between the deuteron beam and the paths of neutrons which can strike the sample, because of the finite dimensions of the neutron source and the sample and the small spacing between them. (The spacing was kept small to maximize the flux.) The spread in neutron energy introduced by this effect is less than that arising from the spread in deuteron energy. Account must also be taken of neutron scattering by that portion of the target backing material, cooling water, water spreader, and catch cage which lies between the source and sample. It is estimated that about 5 percent of the neutrons interact with these materials, the majority losing only a small amount of energy. Since several samples were stacked, account must be taken of neutron scattering by the samples located near the sample in question. This is not considered to be a serious problem in the present experiments, however, because the total thickness (13 mm maximum) was less than the mean-free path of the neutrons (40 mm in Cu, 45 mm in Nb). Neutron scattering by materials at larger distances from the target (e.g. water shielding) does not have a significant effect on the fast neutron spectrum at a sample placed close in because of the rapid decrease of the primary flux with distance from the target.

Because of the relatively sharp nature of this neutron spectrum, it has not been possible to characterize its shape by either threshold foil activation or neutron time-of-flight measurements. The most fruitful approach would appear to be a calculation based upon measured cross sections, deuteron energy loss rates, tritium distribution with depth in the target and the source-sample geometry. This has not been done rigorously for the present experiment, but an indication of the general nature of the shape can be obtained from the calculations of Seagrave[6]. He found that for 400 keV deuterons on a thick tritiated titanium target, the peak in the neutron spectrum in the forward direction (0°) occurs at about 14.8 MeV, and the mean value is also at 15.0 MeV. Taking account of the source-sample geometry in these experiments, we estimate that the mean neutron energy on the face of the Nb was between 14.8 and 15.0 MeV.

The dosimetry for the PCSS irradiations was accomplished by neutron activation and gamma ray counting of nickel foils. The foils were .... cm thick, cut to the same shape as the tensile specimens, and stacked with them so that each tensile specimen was sandwiched between two dosimetry foils. The dose rate during the irradiations was monitored using proton recoil counters, and these data were used to correct for decay. Only the parts of the foils corresponding to the gauge sections on the specimens were weighed and counted, so that the fluences represent average values over the gauge sections. The reaction used was $^{93}Nb(n, 2n)^{92m}Nb$. This reaction has a threshold at about 9 MeV, and the excitation function is relatively flat in the energy region of interest. The cross section value used was 458 millibarns, based upon the measurements of Nethaway[7]. The dosimetry technique has been described by Van Konynenburg[8].

The fluence values shown are the mean values of the fluences calculated for the dosimetry foils in front and in back of each sample. The absolute accuracy of the mean fluences is ±7.5%. Relative accuracy between any two mean fluences is ±2%. The variation of fluence across the thickness of the samples was ±12% of the mean value in the worst cases. The maximum variation of fluence along the length of the gauge section is estimated to be less than ±12% of the mean value for all specimens.

For the room temperature irradiations, the tensile specimens and dosimetry foils were stacked in small epoxy-fiberglass laminate sample holders, and held in place with thin mylar film at front and back. These irradiations were performed in air at about 25°C. Nuclear heating is not significant with this source because the gamma ray flux is quite small. The neutrons are not very effective in heating, as well as having a relatively low flux themselves. This was verified by irradiating a foil mounted in the same way, with a thermocouple spot-welded to its center. The temperature rose less than 3°C when the accelerator was operated. This may have been due in part to a rise in target cooling water temperature, since the foil was pressed against the back of the water catch cage.

The irradiation at 210°C was accomplished by enclosing the samples and dosimetry foils in a Pt capsule and heating them from behind with a spot heater (Research, Inc.)[9]. The Pt capsule was made of 0.75 mm-thick

material, and contained a Pt insert having a slot which conformed to the shape of the specimens. The insert served as a heat sink to ensure temperature uniformity, gave protection against deformation of the samples, and reduced dead space inside the capsule. The capsule was evacuated to a pressure of about 1 mPa (10^{-4} torr) and electron beam welded shut. It was cooled by large copper blocks during the welding operation.

Chromel-alumel thermocouples were spot-welded to the capsule at the side and in the center on the front. The capsule was mounted in an insulator made of firebrick and attached to the front of the spot heater. The front of the capsule was insulated with a 1-cm thick layer of Fiberfrax (3M Co.). The spot heater consists essentially of a tungsten quartz iodide light bulb and an ellipsoidal Al reflector. The bulb was placed at one focus and the capsule at the other. Temperature control was accomplished by use of a current-adjusting type controller and a silicon-controlled rectifier power supply which drove the lamp. Temperature was controlled to within ±5°C during the irradiations. The front of the capsule was measured to be at a temperature of 196°C, and the side at 210°C. The capsule was opened by removing the welded head using a hand shears. Care was taken not to deform the specimens during this operation.

B. Livermore Pool Type Reactor (LPTR)

The LPTR has been described recently[9]. It is a 3 MW heterogeneous tank-type pool research reactor. It is light-water moderated and cooled, beryllium and graphite reflected. It has MTR-type fuel elements, composed of aluminum and enriched uranium. The tensile specimens were irradiated in positions E-1 and E-7 of the reactor core. These positions are located at the northeast and southwest edges of the core, respectively, in the beryllium reflector, adjacent to a large graphite thermal column. Positions E-1 and E-7 have essentially identical environments, from the standpoint of geometry and surrounding materials.

The neutron spectra in these positions have been evaluated by Griffith[10], using multiple foil activation and iterative fitting. The cross sections used in this analysis were taken from McElroy, et al.[11] and from the LLL Evaluated Neutron Data Library. In making the fit, the

lower energy limit was set at 0.025 eV. The main features of these spectra are the fission component above about 10^{-2} MeV and the thermal component below about 1 eV.

In order to minimize thermal neutron activation of the samples, they were surrounded by 0.5-mm thick Cd foil during all LPTR irradiations. It was assumed that the change in the relative shape of the spectrum caused by the Cd can be determined by multiplying the contribution in each energy group by the attenuation averaged over the group as calculated from the Cd cross section. The resulting differential spectra are shown in Figure 4, and the integral spectra in Figure 5. The RTNS spectra are shown for comparison. The LPTR spectra were used to obtain spectrum-averaged cross sections for the reaction $^{54}Fe(n,p)^{54}Mn$, as described by Serpan and Menke[12]. Iron foils were placed next to the tensile samples inside the Cd liner on each run. The absolute fluence values were obtained using the spectrum-averaged cross sections. This procedure accounts for the fact that the Cd lowers the fission rate in the vicinity of the test position relative to the rest of the core. The spectrum-averaged cross sections are shown in Table 2. For comparison, values are shown for position C-53 of the Low Intensity Test Reactor (LITR) (shut down in 1968) and position K-44 of the Brookhaven Graphite Reactor (BGR) (shut down in 1969) from the compilation of Serpan and Menke[12]. The

Table 2.

LOWER ENERGY LIMIT (MeV)	SPECTRUM-AVERAGED CROSS SECTIONS (mb) BGR K-44[12]	LPTR F-1	LITR C-53[12]
>1	69.7	84.8	87.5
>0.1	22.2	28.3	24.6

observation that the present results fall between the others listed is consistent with the fact that the moderation and reflecting material used in the LPTR is a combination of light water and Be as in the LITR, and graphite as in the BGR.

The fluence values determined in this way have an estimated overall uncertainty of ±15% for the >1 MeV values and ±40% for the lower threshold values. It is felt that the fluence variation over the gauge sections of the LPTR samples was much less than that over the RINS samples, because of the volume nature of the neutron source.

As already mentioned, the samples were enclosed in Cd-lined aluminum cans for the irradiation. The cans were cold-welded shut in one atmosphere of air and were vacuum tight. For the 210°C irradiations, the samples were wrapped in Al foil and inserted into the can with little contact with the sides. For the 65°C irradiations, the samples were lightly pressed against a semi-cylinder-shaped Al block, inside the can, using a small spring. The improved thermal contact enabled sufficient heat transfer to the reactor cooling water, which was maintained at 50°C. The temperatures were measured by attaching thermocouples to dummy samples which were irradiated under the same conditions as the actual samples. The temperatures are believed to be accurate to ±10°C. The capsules were opened with a can opener, taking care not to deform the samples.

Tensile Tests

After irradiation and dosimetry measurements were completed the samples were mounted in tensile grips in a specially designed jig to insure against deformation during handling, and tested in an Instron testing machine at or at 25°C and a crosshead rate of 0.05 in/min (0.002 inch/inch-min). Most tests were stopped after about 1 to 2 percent tensile strain so that subsequent TEM examinations of the irradiation damage structures in the gauge sections would not be obscured by dislocations produced by deformation. The 0.2 percent offset yield stress was determined using the instrument crosshead motion as the displacement.

TEM Studies

Transmission electron microscopy studies of the radiation damage structures in the gauge sections of the tensile samples are being carried out to compare the nature and density of the defect structures produced by irradiation at the two temperatures. [illegible]

Thin foils were prepared by slicing the 0.5 mm (0.020-inch) thick gauge sections into two halves approximately 0.2 mm (0.008-inch) thick with a diamond saw. Circular disks 3 mm in diameter were punched or spark cut from these gauge section strips and jet thinned using a 25% concentrated phosphoric acid, 38% distilled water, and 37% ethyl alcohol electrolyte. Structural examinations were carried out on a JEM 100B microscope.

Analysis of the nature of the primary structural defects, i.e., point defect clusters and small dislocation loops, was performed using a new TEM technique called 2-1/2-D. The description of this technique and its application to studies of point defect clusters is in publication[13] and will be briefly described here.

The 2-1/2-D technique utilizes the shifts in dark-field diffraction contrast images produced by off-optical-axis-diffracted beams, when the objective lens is defocused. As shown in the schematic diagram in Figure 6, when a structural feature in a thin foil is imaged by a diffracted beam that makes an angle α with the optical axis of the microscope, and the objective lens is over-focused by lowering the plane of focus relative to the sample position an over-focus distance ΔD, the image position is shifted parallel to the operating reciprocal lattice vector by an amount

$$y = \Delta D\alpha = \Delta D\lambda g \qquad (1)$$

where λ is the electron wave length, g is the distance in reciprocal space of the diffracted beam from the optical axis, and ΔD is positive for over-focusing and negative for under-focusing.

If two photographs of the dark field image are taken at focus settings differing by ΔD, the shift y of the image between the photographs, produced by the off-axis diffracted beam g, causes an artificial parallax that gives the image a depth position when the photographs are viewed in stereo.

When two structural features F_1 and F_2 are simultaneously imaged under high resolution, dark-field conditions, with diffracted beams g_1 and g_2 which make angles α_1 and α_2 with the optical axis of the

microscope as illustrated in Figure 7, and two photographs are taken at objective lens focus settings differing by ΔD, a relative parallax shift of the images will be produced given by

$$\Delta y = y_1 - y_2 = \Delta D(a_2 - a_1) = \Delta D\lambda(g_2 - g_1) = \Delta D\lambda\Delta g \qquad (2)$$

This relative parallax shift will produce a difference P in depth position of the images of F_1 and F_2 when the photographs are viewed in stereo, given by

$$P = M\Delta y \qquad (3)$$

where M is the overall magnification of the photographs.

The difference in stereo depth of the two images of F_1 and F_2 is determined only by Δg or by the difference in spacing or orientation of the diffracting lattice planes and not by the actual positions of F_1 and F_2 in the foil. Consequently, the stereo view is not a true three-dimensional spatial distribution of the features, but neither is it two-dimensional; hence the term 2-1/2-dimensional.

If the two photographs taken at different focus settings are arranged in a stereo viewer with the photograph that is relatively over-focused on the right and the diffraction pattern is as shown in Figure 8a, the image corresponding to the shorter g vector, in this case g_1, will appear in stereo to be above the image corresponding to the longer vector g_2. In this viewing orientation the parallax is caused only by Δg_s or by differences in the spacing of the diffracting lattice planes of features F_1 and F_2, where in this case F_1 would have a larger lattice spacing than F_2. If the photographs are rotated 90 degrees clockwise as illustrated in Figure 8b, the image of feature F_1 will again appear to be above the image of F_2 in stereo. In this case the parallax is produced only by Δg_r or by the difference in rotational orientation of the diffracting planes of features F_1 and F_2.

Application of the 2-1/2-D technique to analysis of point defect clusters is seen by considering an in-focus high-resolution, dark-field micrograph of vacancy and self-interstitial clusters imaged with the [hkl] matrix g vector. The local elastic strains near point defect

clusters produce bending and changes in interplanar spacing of the (hkl) planes as illustrated in Figure 9. Near the interstitial cluster the elastic distortion decreases the (hkl) plane spacing to a value $\bar{d}_{(hkl)i}$ and the vacancy clusters cause a local increase in (hkl) plane spacing to $\bar{d}_{(hkl)v}$. The g vectors corresponding to (hkl) plane diffraction near the vacancy and interstitial clusters $\bar{g}_{(hkl)v}$ and $\bar{g}_{(hkl)i}$ are slightly shorter and longer, respectively, than the $g_{(hkl)}$ vector for the undistorted matrix as shown at the bottom of Figure 9. There is actually a gradient in strain near the clusters and a range of g vectors corresponding to different strains at different points in the matrix. When considering the largest g vector value corresponding to the maximum parallax shift of the defocused dark-field image, a large enough volume of material must be involved to diffract enough electrons to produce an observable dark-field image. Figure 10 shows the (220) plane strain gradients at several radii normal to a 4 nm (40 Å) diameter Frank vacancy loop lying on a (110) plane in niobium. These strains were calculated using the isotropic finite elastic displacement field formulations of Kroupa[14] and Ohr[15]. Consider the volumes of material marked A to E in Figure 10. When the image of the Frank loop is defocused, the images of the volumes A to D that are within about 1 nm (10 Å) of the loop plane, will shift different amounts proportional to the corresponding strain as illustrated in the figure. These volumes are so small that they alone will not diffract enough electrons to produce observable defocused images. At distances greater than about 1 nm (10 Å) from the loop plane, most of the distorted matrix volume marked E in Figure 10, has about the same strain (≈ 4 percent) and will shift the same amount and produce an observable defocused image. Thus, the largest observable image shift for a given lens defocus is expected to correspond to about 4 percent (220) plane strain. This strain has been found to be in good agreement with the values obtained from parallax measurements on tilted-stereo images of this orientation of Frank loops in niobium[13]. The g vector values corresponding to this maximum parallax shift are denoted as $\bar{g}_{(hkl)v}$ and $\bar{g}_{(hkl)i}$.

If a second photograph is taken of the [illegible] clusters under the same [illegible] conditions but with a [illegible] tilted just slightly below the operating $g_{(hkl)}$ vector, the images of the vacancy and interstitial clusters will shift parallel to the operating $g_{(hkl)}$ vector in opposite directions relative to their positions in the in-focus photograph by amounts

$$y_I = z_0(g_{(hkl)I} - g_{(hkl)}) = z_0 \delta g_I \tag{4}$$

$$y_V = z_0(g_{(hkl)V} - g_{(hkl)}) = z_0 \delta g_V \tag{5}$$

giving a net parallax difference

$$\delta y_{IV} = y_I - y_V = z_0(\delta g_I - \delta g_V) = z_0 \delta g_{IV} \tag{6}$$

and a depth difference in stereo of

$$P_{IV} = M \delta y_{IV} \tag{7}$$

When the in-focus and over-focused photographs of the point defect clusters are viewed in stereo with the over-focused photograph on the right and the operating matrix $g_{(hkl)}$ vector directed to the right, the vacancy clusters will appear to be in a depth zone which lies above another depth zone containing interstitial clusters as illustrated in Figure 11. When the photographs are reversed or both are rotated 180 degrees, the interstitial clusters will appear to be above the vacancy clusters. If a crystal matrix [illegible] is used in this [illegible] two beam, it can be [illegible] reference plane, and the true depths of the interstitial and vacancy clusters relative to this plane are given by [illegible] equations (4) - (7). The position of a cluster within a depth zone will be [illegible] as the [illegible] vector.

The result of tilting the [illegible] distorted (kite shaped) [illegible] clusters as can be seen in Figure 12 which is [illegible] position where the [illegible] is tilted to [illegible] $g_{(hkl)}$ axis, the in-focus [illegible] will result [illegible]

similar to the in-focus image, except for a little loss of resolution. The stress [illegible] and below the position where the matrix Bragg angle is [illegible]. Illustrated in Figure 12. Under stronger diffracted beam conditions, the in-focus images are broader and encompass a larger gradient of strain. The out-of-focus images are elongated in the direction of the $\Delta_{(g,\varepsilon)}$ vector and the stress images will appear as tilted plates as shown in Figure 12.

EXPERIMENTAL RESULTS

Radiation Strengthening

The increase in 0.2 percent offset yield stress results are shown vs. neutron fluence in Figures 13 and 14 for Cu and Nb, respectively. Figure 13 shows data for an irradition temperature of 210°C for both neutron spectra and for LPTR irradiations at 65°C and RTNS irradiations at 25°C. Figure 14 shows Nb data for LPTR irradiations at 65°C and RTNS irradiations at 25°C. The increase in yield stress observed for the Cu for a given neutron fluence was independent of the initial material state. In other words, the stores grade Cu had a higher unirradiated yield strength than the Cominco material, but exhibited the same increase in yield stress for a given neutron fluence. The data for the Nb compares fusion neutron irradiated NRC material with fission reactor neutron irradiated LLL stores grade material. LPTR irradiations of the NRC Nb are in progress. The only significant difference between the NRC and LLL stores grade Nb is the higher interstitial content in the latter (see Table 1). Loomis and Gerber[16] have shown that higher concentrations of oxygen impurity significantly increase the radiation strengthening of fission reactor neutron-irradiated Nb. Consequently, the difference in radiation strengthening of the fusion neutron irradiated NRC Nb and the fission reactor neutron-irradiated LLL stores Nb in Figure 14 must be considered less than the difference that would be observed for irradiations of the same material.

It is apparent from these plots that fusion neutrons are considerably more effective than fission reactor neutrons in strengthening both Cu and Nb. If we compare the fusion neutron irradiation of Cu at 21°C

at more elevated temperatures, the ratio would be as great or very possibly greater than the ratio observed at the temperatures in Figure 13.

The radiation strengthening results in Figures 13 and 14 are replotted in Figures 15 and 16 versus damage energy. These plots indicate that at the lower damage states, the radiation strengthening produced by fusion and fission reactor neutrons is approximately equal on a damage energy basis. However, at the higher damage states the strengthening for a given amount of displacement damage produced by fusion neutrons at 25°C is greater than the strengthening for the same amount of damage energy for fission reactor neutrons at 65°C. The ratios of damage energy for fission reactor neutrons to that for fusion neutrons for the same increase in yield strength at the higher damage states is about 2.3 for Cu and 1.6 for Nb. Again, the results at the higher damage states are subject to some uncertainty because of the 40°C difference in irradiation temperature.

Damage Structure Observations

A comprehensive transmission electron microscopy study of the damage structures in the tensile samples used to generate the data in Figures 13 and 14 is in progress and will be reported at a later date. Some initial observations were made of the damage structure in Cu samples irradiated with fusion neutrons to a fluence of 1.27×10^{17} n/cm^2 at 25°C and with fission reactor neutrons to a fluence of approximately 3.0×10^{18} n/cm^2 (E>0.5 eV) at 65°C and 210 C. As can be seen in Figure 13, the fusion neutron and 65°C fission reactor neutron irradiated samples underwent about the same amount of strengthening while the 210°C fission reactor neutron irradiated sample exhibited significantly less strengthening.

Bright-field electron micrographs of the radiation damage structures, which consist of point defect clusters and small dislocation loops, are shown in Figures 17 through 19. It is apparent from these micrographs that there are significant differences between the spatial distributions of the damage clusters in the fusion neutron and fission reactor neutron irradiated samples.

Dark-field 3-D stereo pairs of the fusion neutron and 65°C fission reactor neutron irradiated samples are shown in Figures 20 and 21. The stereo pairs are arranged for viewing with portable or "pocket" stereo viewers. As can be seen in the stereo view of Figure 20, the clusters in the fusion neutron irradiated Cu are uniformly distributed throughout the volume of the foil and range in size from about 1.5 to 10 nm (15 to 100 Å). A number of areas, some of which are shown circled in Figure 20, exhibit close-spaced groups of clusters similar to multiple clusters previously observed in material irradiated with fusion neutrons[17,18,19] and high-energy ions[13,20,21]. The multiple clusters are thought to be produced from multiple cascades created by high-energy primary knock-on events. Although many high-energy primary recoils (>400 keV) do occur in the fusion neutron irradiated Cu, it is not certain whether all of these cluster groups in Figure 20 are multiple clusters. Some of the cluster groups may have resulted from cascade overlap at this fusion neutron fluence. The clusters in the fission reactor neutron-irradiated Cu (Figure 21) have a nonuniform cell-like distribution with cell walls containing a relatively high density of clusters and cell interiors with lower cluster densities. A number of glide dislocations produced during the tensile tests have entangled themselves in the cell wall regions of higher density clusters in the fission reactor neutron irradiated Cu samples.

Estimates of the size-number densities of the clusters in Figures 20 and 21 are shown in Figure 22. The damage in the cell wall regions of the 65°C fission reactor neutron irradiated sample consists of a relatively few large heterogeneously distributed clusters ranging in size from about 7.5 to 20 nm (75 to 200 Å) in diameter and a higher density of smaller clusters about 1.5 to 7.5 nm (15 to 75 Å) in diameter. The interiors of the cells contain a lower density of the smaller clusters. The clusters in the 210°C fission reactor neutron irradiated sample have a distribution similar to that described for the 65°C irradiated sample except that there is an overall reduction in the small cluster density and the larger clusters have grown into resolvable loops 20 to 50 nm (200 to 500 Å) in diameter. The number-density of observed clusters in the fusion neutron irradiated sample is substantially greater

than the cluster density in the cell interiors of the 65°C fission reactor [illegible] cell walls. Since the [illegible] tenth as large as the fission reactor neutron flux (E>0.1 MeV), it appears reasonable to conclude that the rate of accumulation of displacement damage in the form of point defect clusters during irradiation with fusion neutrons is significantly greater than that during irradiation with fission reactor neutrons. This conclusion is in agreement with the results of earlier studies of fusion neutron damage in Cr[17], Nb[18], and Mo[22].

Figures 23 and 24 are 2-1/2-D stereo pairs of the same areas of the fusion and 65°C fission reactor neutron irradiated samples shown in Figures 20 and 21. The micrographs are arranged so that in stereo the vacancy clusters appear above the interstitial clusters. The 2-1/2-D depth distributions of the clusters produced by the fusion and fission reactor neutrons are the same and are shown in Figure 25. The depth positions Va and Ia correspond to vacancy and interstitial clusters with a/3 ⟨111⟩ Burgers vectors and the positions Vb and Ib to clusters with a/2 ⟨110⟩ Burgers vectors. Several clusters in Figures 23 and 24 are so indicated. These Burgers vectors are consistent with those determined from the direction of the axes of the black-white lobes of the dynamical images of the clusters, examples of which are shown in Figures 26 and 27. It can be seen by inspection of the 2-1/2-D stereo view of Figure 24 that the majority of the smaller clusters (<7.5 nm (75 Å) in diameter) in the fission reactor neutron irradiated sample are vacancy-type with predominantly a/3 ⟨111⟩ Burgers vectors while nearly all of the larger clusters (>7.5 nm (75 Å) in diameter) are interstitial-type with many having a/2 ⟨110⟩ Burgers vectors. Inspection of the 2-1/2-D stereo pair of the fusion neutron irradiated specimen (Figure 23) reveals that the interstitial clusters are randomly distributed with the vacancy clusters. The largest clusters observed in this micrograph are interstitial type, but in general the size distribution of the interstitial clusters is similar to that of the vacancy clusters.

The inhomogeneous distribution of the large interstitial clusters in the fission reactor neutron-irradiated samples suggests that they

multiple clusters. The majority of clusters formed during fission reactor neutron irradiation, on the other hand, appear to develop from the diffusion-controlled coalescence of interstitials and excess vacancies. The fraction of the displacement damage retained in the form of point defect clusters appears to be greater during fusion neutron irradiation than during fission reactor neutron irradiation primarily because of the increased recombination of the diffusing vacancies and interstitials during fission reactor neutron irradiation.

REFERENCES

1. R. BOOTH, IEEE Trans. Nucl. Sci. NS14, 993 (1967).
2. R. BOOTH and H. H. BARSCHALL, Nucl. Instrum. Methods 99, 1 (1972).
3. R. BOOTH, H. H. BARSCHALL, and E. GOLDBERG, IEEE Trans. Nucl. Sci. NS20, 472 (1973).
4. R. BOOTH, Nucl. Instrum. Methods 120, 353 (1974).
5. R. A. VAN KONYNENBURG, H. H. BARSCHALL, R. BOOTH, and C. WONG, Proc. Int'l Conf. on Radiation Test Facilities for the CTR Surface and Materials Program, Argonne National Laboratory, July 15-18, 1975 (to be published).
6. J. SEAGRAVE, D(d,n)^{3}He and T(d,n)^{4}He Neutron Source Handbook, LAMS-2162, Los Alamos Scientific Laboratory (1957).
7. D. HETHERAY, Nucl. Phys. A190, 635 (1972) and personal communication of later results (Feb. 1975).
8. R. A. VAN KONYNENBURG, Neutron Dosimetry (14 MeV) for Foil Samples Irradiated with the Lawrence Livermore Laboratory Rotating Target Neutron Source, UCRL-51393 Rev. 1, Lawrence Livermore Laboratory (1974).
9. LAWRENCE LIVERMORE LABORATORY, Safety Analysis Report for Livermore Pool Type Reactor, UCRL-51423 (1974).
10. R. V. GRIFFITH, "Activation Foil Neutron Spectra in the Core of the LPTR," in Hazards Control Progress Report No. 49 - July through December 1974, UCRL-50007-74-2, Lawrence Livermore Laboratory (1975).
11. W. N. McELROY and S. BERG, A Computer-Automated Iterative Method for Neutron Flux Spectra Determination by Foil Activation, Kirtland AFB Report AFWL-TR-67-41, 4 (1967).
12. C. Z. SERPAN, JR., and H. H. HEMMY, "Nuclear Reactor Neutron Energy Spectra," ASTM Data Series Publication, Amer. Soc. for Testing and Materials, Philadelphia (1974).
13. J. B. MITCHELL and M. L. BELL, "Characterization of Point Defect Clusters by 2-1/2-D FIM," (to be published in Acta Met. 1975).
14. F. KROUPA, Czech. J. Phys. 10, 284 (1960).
15. S. M. COX, Phil. Mag. 26, 1307 (1972).
16. B. A. LOOMIS and S. B. GERBER, Acta Met. 21, 165, (1973).
17. J. B. MITCHELL, D. M. LOOMA, and C. J. ECHER, J. Nucl. Matls. 48, 139, (1973).
18. J. B. MITCHELL, B. A. [illegible], M. M. [illegible], and C. J. ECHER, Phil. Mag. 31, 919 (1975).
19. K. L. MERKLE, Nucl. [illegible], 22, [illegible] (1973).

20. K. L. MERKLE, Proc. of the Vienna Symposium on Radiation Damage in Radiation Damage in Reactor Materials (Vienna: International Atomic Energy Agency), 59 (1969).

21. F. HAUSSERMANN, Phil. Mag. 25, 537 (1972).

22. J. L. BRIMHALL, L. A. CHARLOT, and H. E. KISSINGER, "14 MeV Neutron Damage in Molybdenum," (to be published in Radiation Effects 1975).

† Reference to company or product name here and elsewhere in this report does not imply approval or recommendation of the product or company by the University of California or the U. S. Energy Research Development Administration to the exclusion of others that may be suitable.

ACKNOWLEDGEMENTS

This work was performed under the auspices of the U. S. Energy Research and Development Administration, * The samples were prepared by Fay Dishong and Gene Raymond. RTNS irradiation were performed by Donald Rawles, Lewis Mego, Richard Penprase, and Rex Booth. LPTR irradiations were performed by Wade Richards, Joe Prindle, and Will Burns. Ruth Anderson and Susan MacLean carried out the gamma-ray counting and dosimetry calculations, respectively. Fran Silva encapsulated the higher temperature specimens. Robert Hibbard designed the irradiation furnace. Curtis Rowe gave assistance in setting up and monitoring irradiations. All this help is gratefully appreciated.

*Under contract No. W-7405-Eng-48

FIGURE LIST

Caption

Fig. 1. Tensile Sample Dimensions.

Fig. 2&3. Representative Microstructures of Nb and Cu Tensile Samples.

Fig. 4. Differential Neutron Spectra for the E-1 and E-7 Positions of the LPTR Fission Reactor.

Fig. 5. Integral Neutron Spectra for the E-1 and E-7 Positions of the LPTR Fission Reactor.

Fig. 6. Schematic Diagram Showing Image Shift Produced by Over-focusing the Objective Lens Under Dark-Field Conditions.

Fig. 7. Diffraction Pattern Arrangement for Taking 2-1/2-D Stereo Pair of Features F_1 and F_2.

Fig. 8. Stereo Setup for 2-1/2-D Viewing.

Fig. 9. Illustration of Lattice Strains Produced by Vacancy and Interstitial Point Defect Clusters or Dislocation Loops.

Fig. 10. Illustration of Strain Gradients and Defocusing Image Shifts Near a Frank Vacancy Loop.

Fig. 11. Schematic Illustration of Vacancy and Interstitial Cluster Distributions in 2-1/2-D Stereo Space.

Fig. 12. Illustration of the 2-1/2-D Stereo Images of Clusters for Weak-Beam and Strong-Beam Dark-Field Conditions.

Fig. 13. Increase in Tensile Yield Stress Versus Neutron Fluence in Copper.

Fig. 14. Increase in Tensile Yield Stress Versus Neutron Fluence in Niobium.

Fig. 15. Increase in Tensile Yield Stress Versus Damage Energy for Neutron Irradiated Copper.

Fig. 16. Increase in Tensile Yield Stress Versus Damage Energy in Neutron Irradiated Niobium.

Fig. 17. Bright-Field Transmission Electron Micrograph of Fusion

Neutron Radiation Damage in Cu, $\emptyset t = 1.27 \times 10^{17} n/cm^2$, 25°C.

Fig. 18. Bright-Field Transmission Electron Micrograph of Fission Reactor Neutron Damage in Copper $\emptyset t = 3.3 \times 10^{18} n/cm^2$, E>0.5 eV, 65°C.

Fig. 19. Bright-Field Transmission Electron Micrograph of Fission Reactor Neutron Radiation Damage in Copper, $\emptyset t = 2.51 \times 10^{18} n/cm^2$, E>0.5 eV, 210°C.

Fig. 20. Dark-Field 3-D Stereo Micrographs of Fusion Neutron Damage in Copper, $\emptyset t = 1.27 \times 10^{17} n/cm^2$, 25°C, B = [001], g = [400].

Fig. 21. Dark-Field 3-D Stereo Micrographs of Fission Reactor Neutron Damage in Copper, $\emptyset t = 3.3 \times 10^{18} n/cm^2$, E>0.5 eV, 65°C, B = [001], g = [400].

Fig. 22. Size-number Density Distributions of Clusters in Fusion Neutron and 65°C Fission Reactor Neutron Irradiated Copper.

Fig. 23. Dark-Field 2-1/2-D Stereo Micrograph of Fusion Neutron Irradiated Copper of Fig. 20, $\Delta D = 2\mu m$.

Fig. 24. Dark-Field 2-1/2-D Stereo Micrographs of 65 C Fission Reactor Neutron Irradiated Copper of Fig. 21, $\Delta D = 2\mu m$.

Fig. 25. Stereo 2-1/2-D Depth Distribution of Cluster Images of Fusion and Fission Reactor Neutron Irradiated Copper.

Fig. 26. Dynamical Contrast Micrographs of Clusters in Fusion Neutron Irradiated Copper.

Fig. 27. Dynamical Contrast Micrograph of Clusters in 65°C Fission Reactor Neutron Irradiated Copper.

FIGURE 1

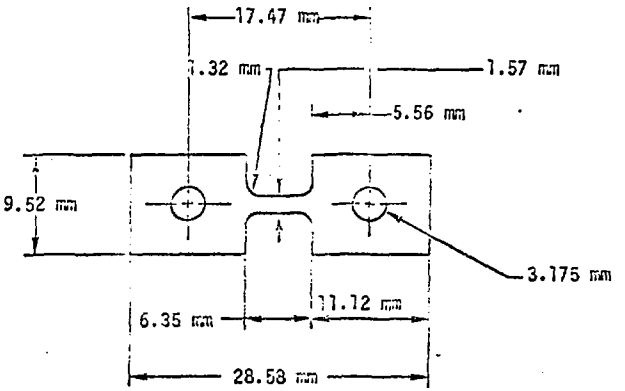

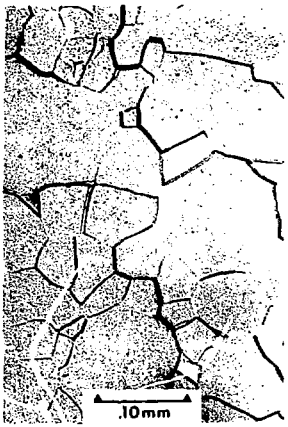

Figure 2

Figure 3

FIGURE 4

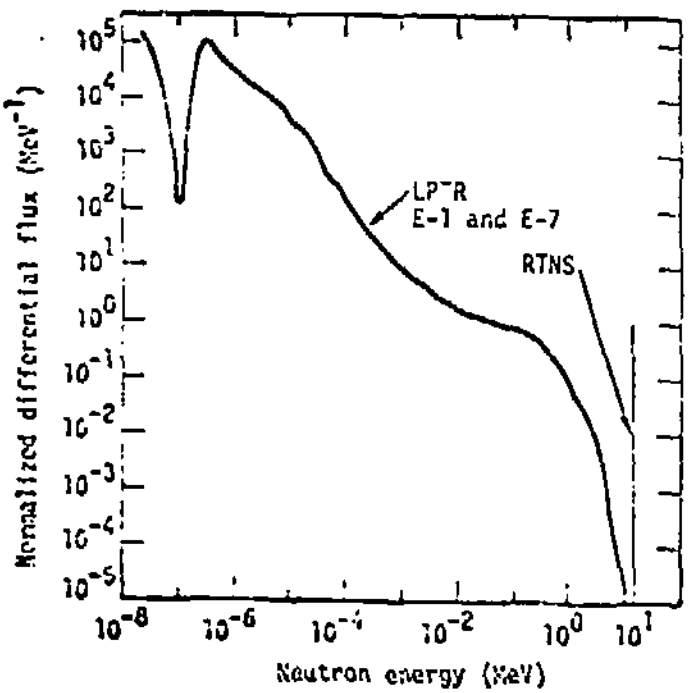
Normalized differential flux (MeV^{-1})
10^{5}
10^{4}
10^{3}
10^{2}
10^{1}
10^{0}
10^{-1}
10^{-2}
10^{-3}
10^{-4}
10^{-5}
LPTR
E-1 and E-7
RTNS
10^{-8}
10^{-6}
10^{-4}
10^{-2}
10^{0}
10^{1}
Neutron energy (MeV)

FIGURE 5

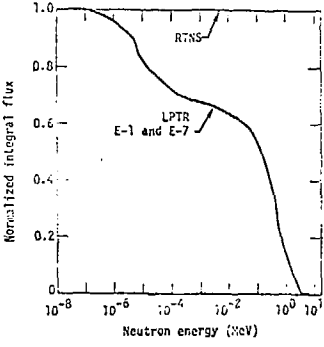
1.0
0.8
0.6
0.4
0.2
0
Normalized integral flux
RTNS
LPTR
E-1 and E-7
10^{-8}
10^{-6}
10^{-4}
10^{-2}
10^{0}
10^{1}
Neutron energy (MeV)

FIGURE 6

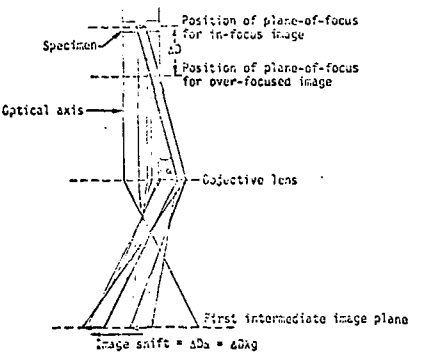
Position of plane-of-focus
for in-focus image
Specimen
Δ
Position of plane-of-focus
for over-focused image
Optical axis
Objective lens
First intermediate image plane
Image shift = ΔDa = ΔDag

FIGURE 7

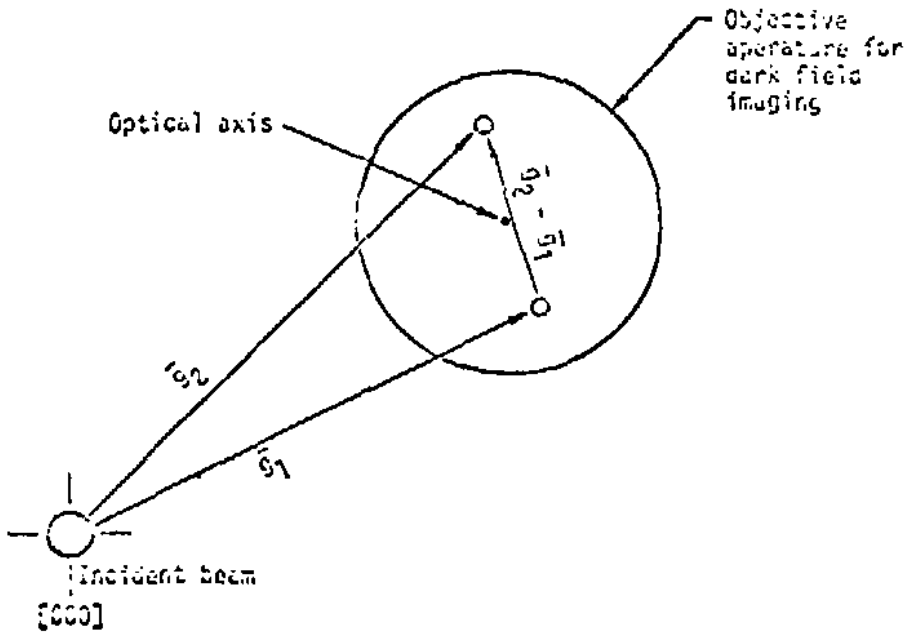
Objective aperture for dark field imaging
Optical axis
$\vec{g}_2 - \vec{g}_1$
$\vec{g}_2$
$\vec{g}_1$
Incident beam
[000]

FIGURE 8

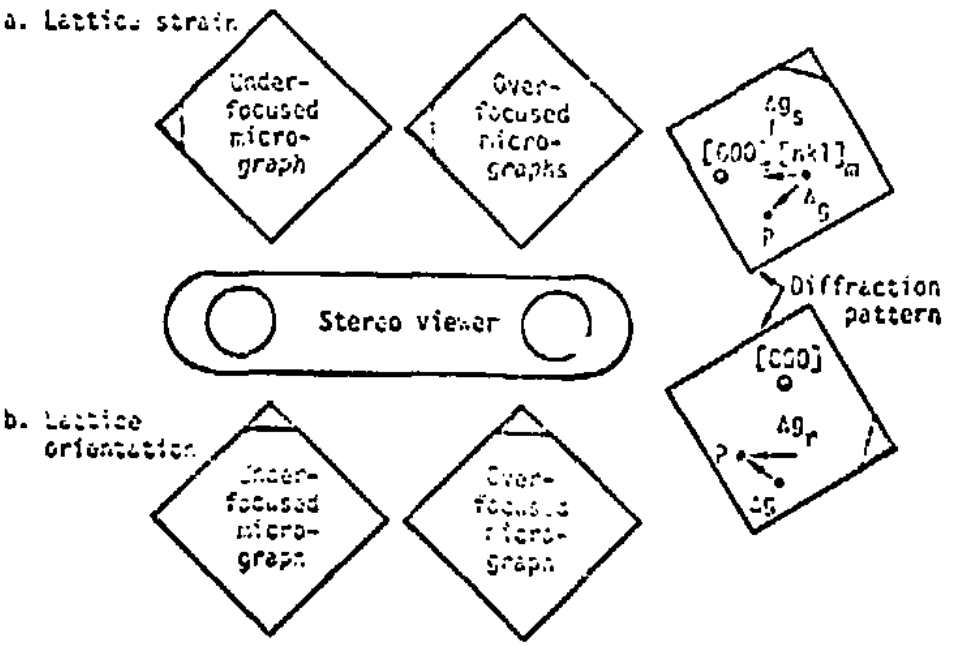
a. Lattice strain
Under-focused micro-graph
Over-focused micro-graphs
Stereo viewer
Diffraction pattern
b. Lattice orientation
Under-focused micro-graph
Over-focused micro-graph

FIGURE 9

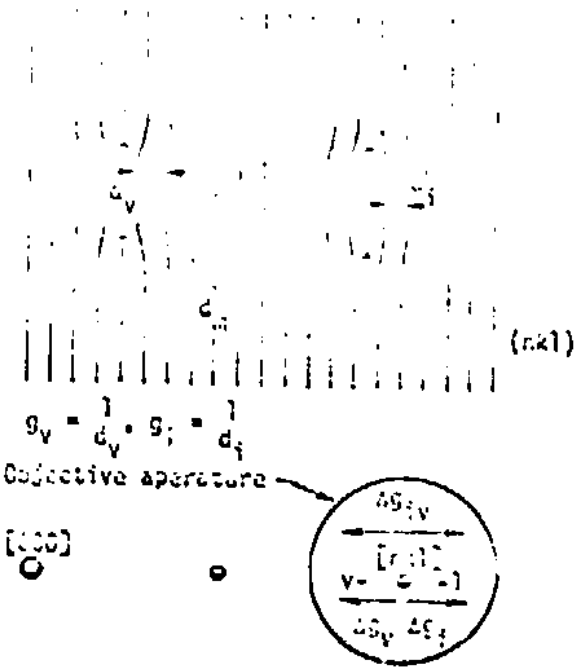

FIGURE 10

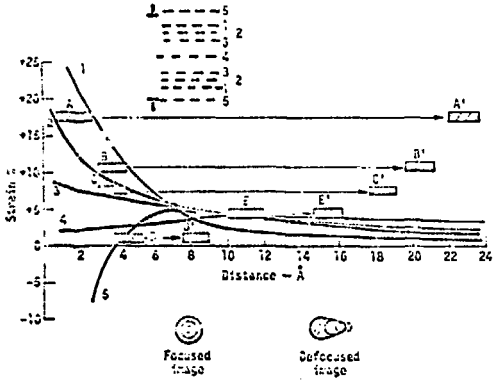
1
5
2
3
4
3
2
1
5
+25
+20
+15
+10
+5
0
-5
-10
Strain %
A
A'
B
B'
C
C'
D
D'
E
E'
1
2
3
4
5
2
4
6
8
10
12
14
16
18
20
22
24
Distance — Å
Focused image
Defocused image

FIGURE 11

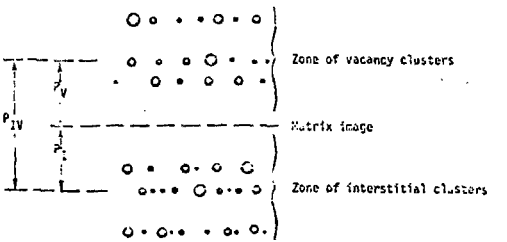
Zone of vacancy clusters
Matrix image
Zone of interstitial clusters

FIGURE 12

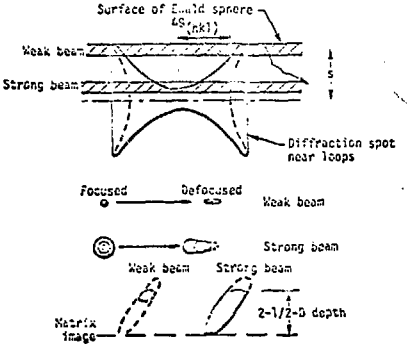
Surface of Ewald sphere
$\Delta S_{(hkl)}$
Weak beam
Strong beam
Diffraction spot
near loops
Focused
Defocused
Weak beam
Strong beam
Weak beam
Strong beam
Matrix
image
2-1/2-D depth

FIGURE 13

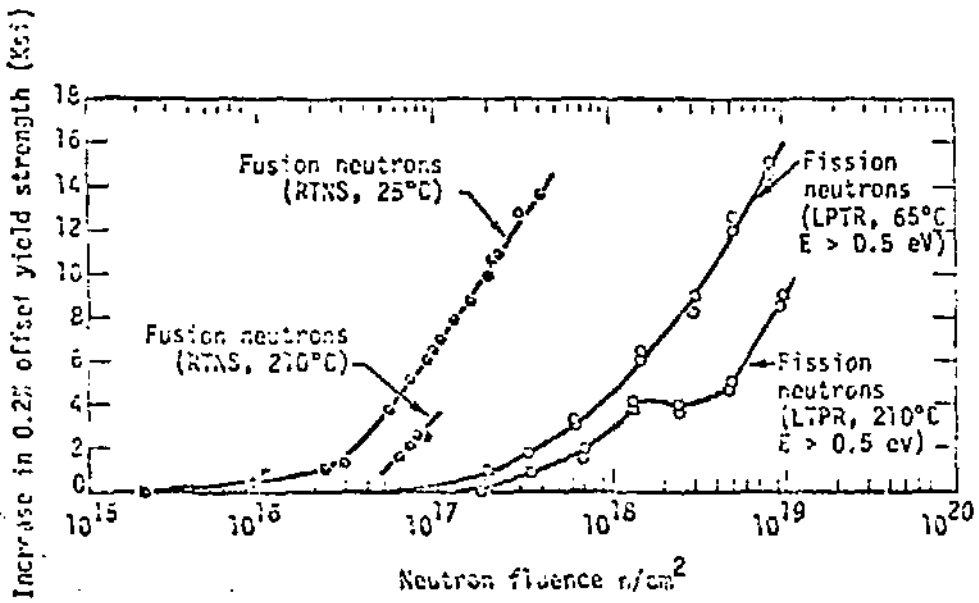
Increase in 0.2% offset yield strength (Ksi)
18
16
14
12
10
8
6
4
2
0
Fusion neutrons
(RTNS, 25°C)
Fusion neutrons
(RTNS, 210°C)
Fission
neutrons
(LPTR, 65°C
E > 0.5 eV)
Fission
neutrons
(LTPR, 210°C
E > 0.5 ev)
10^{15}
10^{16}
10^{17}
10^{18}
10^{19}
10^{20}
Neutron fluence n/cm^2

FIGURE 14

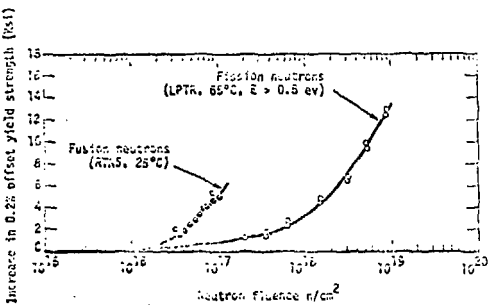
Increase in 0.2% offset yield strength (ksi)
Fission neutrons
(LPTR, 65°C, E > 0.5 ev)
Fusion neutrons
(RTNS, 25°C)
Specimens
Neutron fluence n/cm²

FIGURE 15

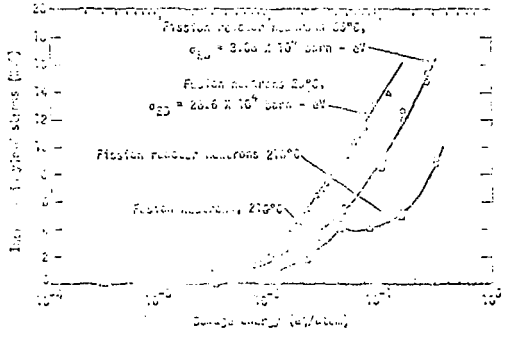

FIGURE 16

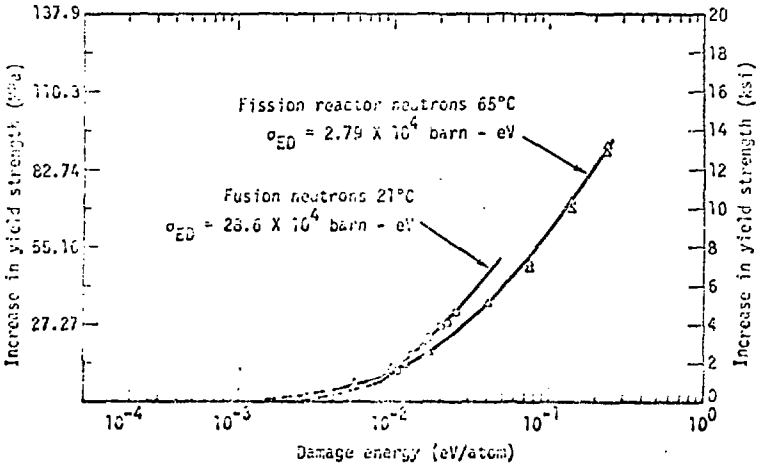
137.9
110.3
82.74
55.16
27.27
Increase in yield strength (MPa)
20
18
16
14
12
10
8
6
4
2
0
Increase in yield strength (ksi)
Fission reactor neutrons 65°C
σ_{ED} = 2.79 X 10^4 barn - eV
Fusion neutrons 21°C
σ_{ED} = 28.6 X 10^4 barn - eV
10^{-4}
10^{-3}
10^{-2}
10^{-1}
10^{0}
Damage energy (eV/atom)

Figure 17

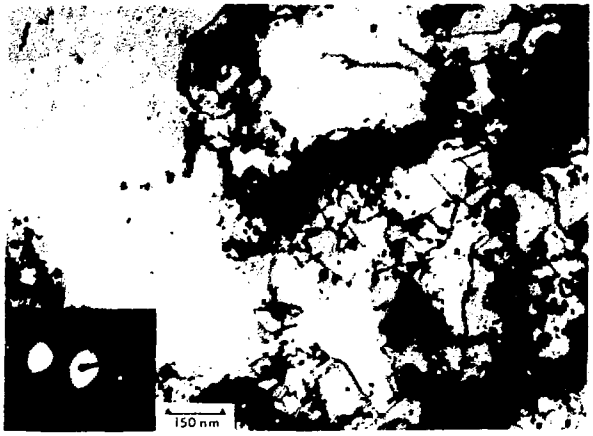

Figure 18

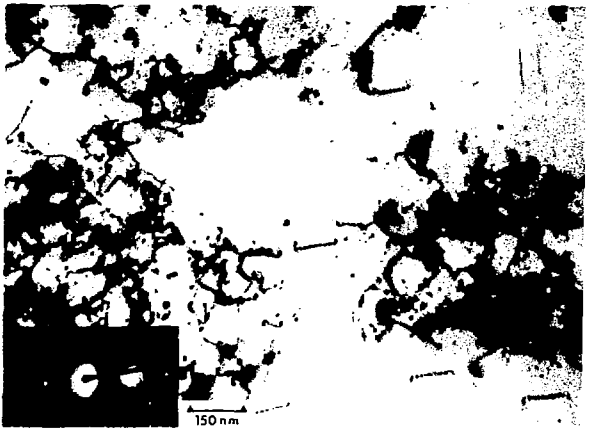

Figure 19

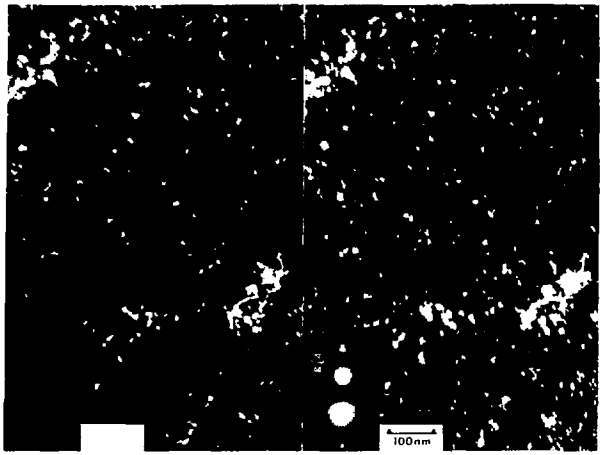

Figure 20

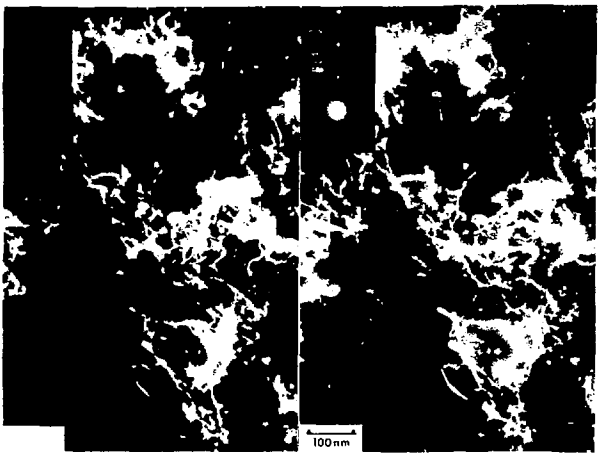

Figure 21

FIGURE 22

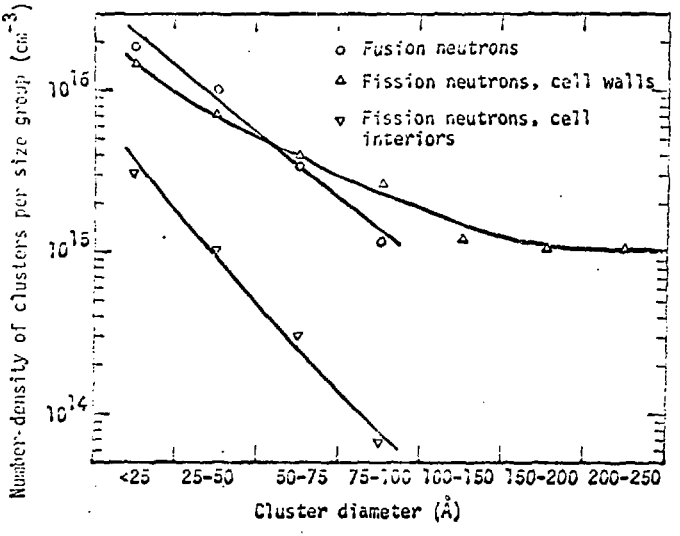
Number-density of clusters per size group (cm^{-3})
10^{16}
10^{15}
10^{14}
o Fusion neutrons
Δ Fission neutrons, cell walls
▽ Fission neutrons, cell interiors
<25
25-50
50-75
75-100
100-150
150-200
200-250
Cluster diameter (Å)

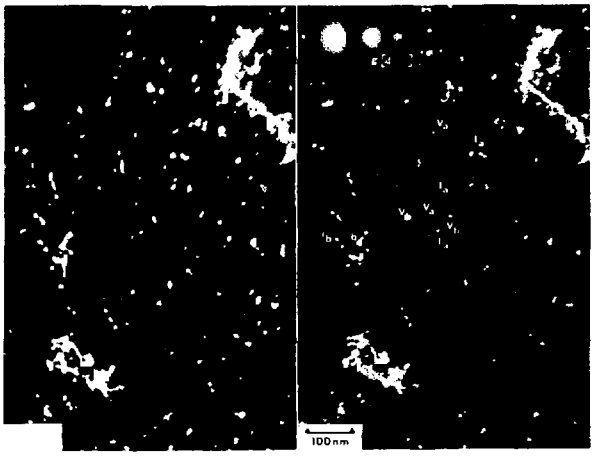

Figure 53

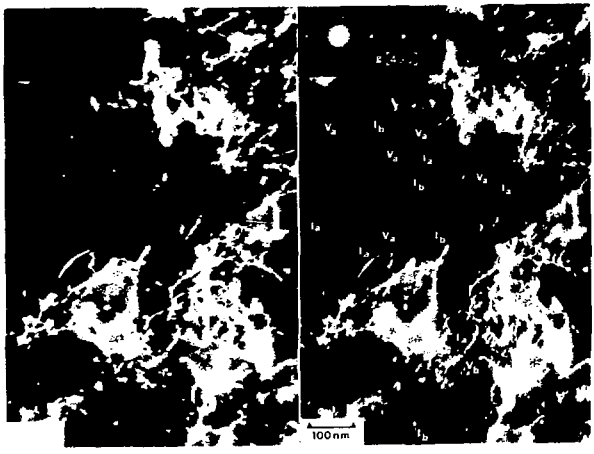

Figure 54

FIGURE 25

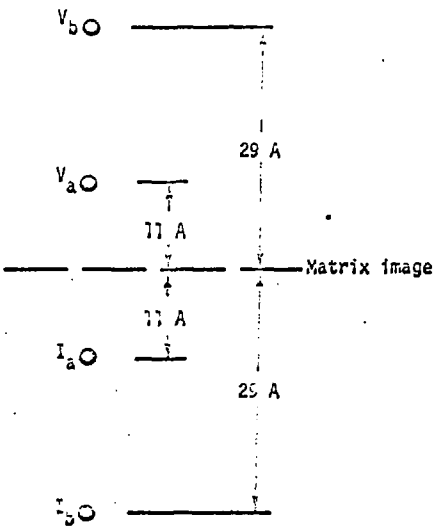

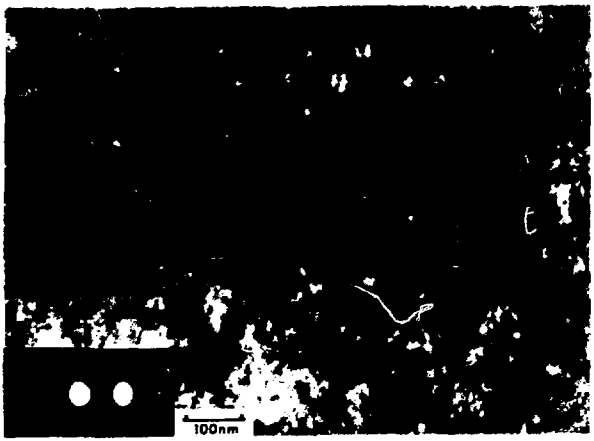

Figure 1a

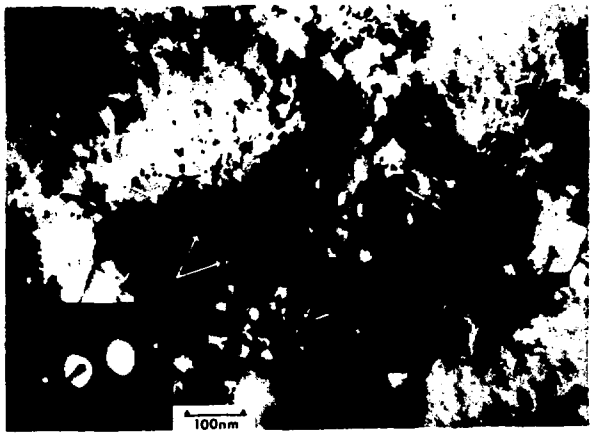

Figure 1b